Biomaterials 35 (2014) 1608–1617

Contents lists available at ScienceDirect

Biomaterials

journal homepage: www.elsevier.com/locate/biomaterials

Magnetically engineered Cd-free quantum dots as dual-modality probes for fluorescence/magnetic resonance imaging of tumors

Ke Ding, Lihong Jing*, Chunyan Liu, Yi Hou, Mingyuan Gao*

Institute of Chemistry, Chinese Academy of Sciences, Bei Yi Jie 2, Zhong Guan Cun, Beijing 100190, China

ARTICLE INFO

Article history:
Received 12 September 2013
Accepted 27 October 2013
Available online 15 November 2013

Keywords:
Cd-free $CuInS_2$@ZnS:Mn QDs
Cytotoxicity
Fluorescence/MR dual-modality probe
Tumor imaging
In vivo

ABSTRACT

Magnetically engineered Cd-free $CuInS_2$@ZnS:Mn quantum dots (QDs) were designed, synthesized, and evaluated as potential dual-modality probes for fluorescence and magnetic resonance imaging (MRI) of tumors *in vivo*. The synthesis of Mn-doped core–shell structured $CuInS_2$@ZnS mainly comprised three steps, i.e., the preparation of fluorescent $CuInS_2$ seeds, the particle surface coating of ZnS, and the Mn-doping of the ZnS shells. Systematic spectroscopy studies were carried out to illustrate the impacts of ZnS coating and the following Mn-doping on the optical properties of the QDs. In combination with conventional fluorescence, fluorescence excitation, and time-resolved fluorescence measurements, the structure of $CuInS_2$@ZnS:Mn QDs prepared under optimized conditions presented a Zn gradient $CuInS_2$ core and a ZnS outer shell, while Mn ions were mainly located in the ZnS shell, which well balanced the optical and magnetic properties of the resultant QDs. For the following *in vivo* imaging experiments, the hydrophobic $CuInS_2$@ZnS:Mn QDs were transferred into water upon ligand exchange reactions by replacing the 1-dodecanethiol ligand with dihydrolipoic acid-poly(ethylene glycol) (DHLA-PEG) ligand. The MTT assays based on HeLa cells were carried out to evaluate the cytotoxicity of the current Cd-free $CuInS_2$@ZnS:Mn QDs for comparing with that of water soluble CdTe QDs. Further *in vivo* fluorescence and MR imaging experiments suggested that the PEGylated $CuInS_2$@ZnS:Mn QDs could well target both subcutaneous and intraperitoneal tumors *in vivo*.

1. Introduction

Molecular imaging has stimulated intense interest as it will surely offer revolutionary tools not only for fundamental studies but also for clinical applications. The dilemma of imaging modality selection in the clinic is that each modality has its own unique advantages and intrinsic limitations, such as insufficient sensitivity or low spatial resolution, so it remains difficult to extract accurate and reliable biomedical information solely based on single imaging modalities [1,2]. Integrating the advantages of different imaging techniques is apparently an effective approach for improving the efficacy of clinical imaging diagnosis [3–5]. To date, the combinations of different imaging methods such as positron emission tomography (PET)/computed tomography (CT) [6] and PET/magnetic resonance imaging (MRI) [7] have already developed into commercial imaging instruments being adopted clinically. Although the optical imaging techniques have shown potentials in extracting detailed biomedical information with high imaging sensitivities and low cost in imaging facilities, the assist of anatomical information is essentially required. In this context, the combination of optical imaging techniques and MRI may represent another useful imaging modality pair for more accurate biomedical detections.

Nanoparticle provides an ideal platform for developing novel fluorescence/MR dual-modality probes especially for tumor imaging [3,4,8–10]. Different strategies have been developed towards this goal by integrating fluorescent quantum dots (QDs) with magnetic nanoparticles or individual magnetic ions for forming bifunctional nanoparticles, including epitaxial heterocrystalline growth, co-encapsulation of pre-made magnetic particle and QD, conjugation of magnetic chelates to QD, and doping QDs with transition metal ions, *etc*. The epitaxial heterocrystalline growth is commonly realized by directly coating superparamagnetic nanoparticles such as FePt, γ-Fe_2O_3, and Co nanocrystals with II–VI semiconducting materials for fusing them into either spherical core/shell particles or hetero-dimers [11–13]. However, the fluorescence quantum yield (QY) of the resultant bifunctional particles is generally low, typically below 5%, due to the quenching effect of the magnetic domains [11–13]. In contrast, bifunctional particles with QY higher than 10% can be obtained by encapsulating pre-made magnetic nanoparticles and QD into inert matrices such as silica or polymer [14–16]. Nonetheless, the resultant composite particles are typically larger than 50 nm and prone to higher uptake by the reticuloendothelial system (RES) in comparison with small

* Corresponding authors. Fax: +86 10 8261 3214.
E-mail addresses: jinglh@iccas.ac.cn (L.H. Jing), gaomy@iccas.ac.cn (M.Y. Gao).

0142-9612/$ – see front matter © 2013 Elsevier Ltd. All rights reserved.
http://dx.doi.org/10.1016/j.biomaterials.2013.10.078

counterparts. In contrast, coating QDs directly with paramagnetic metal chelates such as Gd chelates by self-assembly or covalent coupling is more favorable for achieving magnetic QDs without largely increasing the overall size of the particles [17–20]. Moreover, the presence of the paramagnetic metal chelates on the surface of QDs is in favor of T_1-weighted MR imaging. Nevertheless, the high binding affinity of the chelating ligand may heavily etch the QDs before it coordinates with the paramagnetic metal ions for forming the magnetic metal chelates on the QD surface [19,20].

Contrasting to the aforementioned methods, doping QDs with paramagnetic metal ions for achieving intrinsically paramagnetic QDs is superior because the overall size of the bifunctional particles can greatly be decreased down to <5 nm [21,22]. The small size of the particles is in favor of fast excretion of the intravenously administrated particle probes, largely reducing the possible side effects of the QDs within the body. Until now, doping II–VI QDs such as Cd(S, Se) [23–27], Zn(S, Se) [28–32] with Mn has been demonstrated to be a reliable approach for achieving fluorescence/magnetic bifunctional particles that can potentially be used for fluorescence/MR dual-modality imaging. The cytotoxicity of Cd^{2+} is an unavoidable problem for transferring the imaging probes to the clinic [33,34], although cadmium chalcogenide QDs are characterized by unique fluorescent properties [35–40] owing to their suitable exciton Bohr radii. In this context, zinc chalcogenide QDs are taken as suitable alternatives with respect to toxicities [28,32]. But their smaller exciton Bohr radii require the excitation photons to have much higher energy with wavelength typically below 400 nm. Apart from optical damage to tissue, the tissue penetration depth of the excitation light for exciting zinc chalcogenides nanoparticles is much limited [4].

Recent investigations suggest that I–III–VI QDs, such as $CuInS_2$ QDs, are very promising Cd-free candidates for *in vivo* applications [41–43], because they can be excited by incident light with wavelength up to 600 nm. Moreover, the photoluminescence (PL) emission covers a wide range from visible to near-infrared (NIR) with fluorescence QY up to 60% under optimized conditions if coated by ZnS shell [44–50]. Therefore, the magnetically engineered $CuInS_2$-based quantum dots may hold great potentials for producing fluorescence/MR dual-modality molecular imaging probes with greatly suppressed toxicity and suitable optical properties for *in vivo* imaging of tumors.

Following on from our previous studies on $CuInS_2$ nanocrystals [44] and *in vivo* tumor imaging based on versatile magnetic tumor probes [51–53], herein we report a new Cd-free dual-modality imaging probe constructed by doping ZnS coated $CuInS_2$ dots with Mn for achieving highly fluorescent and magnetic QDs. The ZnS coating has twofold functions in the designed particles, on the one hand, it was used to increase the fluorescence QY of the $CuInS_2$ core, on the other hand to reduce the fluorescence quenching effect caused by Mn-doping. Therefore, the impacts of the ZnS coating and the following Mn-doping on the optical properties of the $CuInS_2$ dots were systematically studied. A poly(ethylene glycol) (PEG) based hydrophilic ligand was designed and used for rendering resultant nanoparticles water soluble through ligand exchange. The optical and magnetic properties of the resultant bifunctional QDs were investigated and preliminary tumor imaging studies were carried out for showing their potential for detecting tumors *in vivo*.

2. Materials and methods

2.1. Chemicals

Indium(III) acetate ($In(OAc)_3$, 99.99%) was purchased from Alfa Aesar. 1-dodecanethiol (DDT, 97%) was purchased from Sigma-Aldrich. Copper(I) iodide (CuI, 99.995%), manganese(II) chloride tetrahydrate ($MnCl_2{\cdot}4H_2O$, 99%), stearic acid (SA, 98%), Zinc stearate ($ZnSt_2$) (90%) were purchased from Aladdin. DHLA-PEG2000 ligand was customized product provided by Beijing Oneder Hightech Co. Ltd. Acetone, cyclohexane, methanol, tetrahydrofuran, ether, dichloromethane, hydrochloric acid, and toluene were analytical reagent grade and purchased from Sinopharm Chemical Reagent Beijing, Co., Ltd. 3-(4,5-dimethylthiazol-2-yl)-2,5-diphenyl tetrazolium bromide (MTT, 98%), dimethyl sulfoxide (DMSO), Dulbecco's Modified Eagle Medium (DMEM, high glucose), and fetal bovine serum (FBS) were bought from Biodee Biotechnology Co., Ltd., Beijing, China. Other solvents and chemicals were used without further purification.

2.2. Synthesis of Mn stearate ($MnSt_2$)

In a typical synthesis of Mn precursor [28], 2.84 g (10 mmol) of SA was dissolved in 15 mL of methanol. The resultant mixture was heated to 50–60 °C to form a homogeneous solution. After the reaction system was cooled down to the room temperature, 20 mL of methanol solution containing 0.91 g (10 mmol) of TMAH was introduced, and then the mixture was kept under stirring for 15 min. Subsequently, 10 mL of methanol solution containing 0.99 g (5 mmol) of $MnCl_2{\cdot}4H_2O$ was dropwise introduced into the above mixture under vigorous stirring, which generated white $MnSt_2$ precipitates that were collected by centrifugation, washed by methanol for several times and then dried under vacuum. The final product was stored under N_2 protection before further use.

2.3. Synthesis of $CuInS_2$ seeds QDs

The $CuInS_2$ seeds were prepared according to a slightly modified method previously reported [44,47]. In brief, 0.0584 g (0.2 mmol) of $In(OAc)_3$ and 0.038 g (0.2 mmol) of CuI were mixed with 12 mL of 1-dodecanethiol. The reaction mixture was firstly degassed under vacuum for 30 min, and then nitrogen gas was introduced to purge the reaction solution. After 30 min, the resultant mixture was heated to 200 °C, and the reaction was allowed for 120 min under nitrogen protection. During this process, the reaction mixture changed from turbid white to transparent yellow when the reaction temperature reached 160 °C and then remained transparent throughout the reaction. In the meantime, the color of the reaction solution progressively changed from light yellow to yellow, red, and finally dark brown. The $CuInS_2$ QDs were precipitated by acetone and isolated by centrifugation, redispersion in cyclohexane, and subsequent precipitation by using acetone for three cycles, the nanocrystals finally obtained were redispersed in cyclohexane for further experiments.

2.4. Synthesis of $CuInS_2$@ZnS QDs

Following the aforementioned procedures for synthesizing $CuInS_2$ seeds, a parallel reaction mixture was prepared by 120 min reaction at 200 °C. Without applying the purification procedures, 0.632 g (1.0 mmol) of $ZnSt_2$ was introduced at room temperature. The resultant reaction mixture was then heated up to 230 °C to initiate the ZnS coating process. A series of aliquots were extracted at 230 °C for monitoring the particle growth. The purification procedures for the collected particles were the same as those described above.

In parallel, one more sample was prepared by introducing 0.253 g (0.4 mmol) instead of 0.632 g (1.0 mmol) $ZnSt_2$ into a parallel reaction system for producing $CuInS_2$ QDs with thinner ZnS coating layer following the procedures mentioned above.

2.5. Synthesis of $CuInS_2$@ZnS:Mn QDs

Following the aforementioned procedures for synthesizing $CuInS_2$@ZnS QDs, a parallel reaction mixture was prepared by 120 min reaction at 230 °C. Without applying the purification procedures, 2 mL of DDT solution containing 0.124 g (0.2 mmol) of $MnSt_2$ was introduced when the reaction mixture was cooled down to 180 °C to initiate the Mn-doping process. A series of aliquots were extracted at 180 °C for monitoring the doping process. The purification procedures for the collected particles were the same as those described above. The sample obtained by 180 min of reaction, i.e., sample A, was used in the following experiments.

In parallel, two more sample was prepared, i.e., sample B and sample C. Sample B was prepared by using 0.311 g (0.5 mmol) instead of 0.124 g (0.2 mmol) $MnSt_2$. By the same procedures for sample A, sample C was prepared based on $CuInS_2$@ZnS QDs with thinner ZnS shell.

2.6. PEGylated $CuInS_2$@ZnS:Mn QDs

100 mg of hydrophobic $CuInS_2$@ZnS:Mn QDs were mixed with 1 g of DHLA-PEG in 50 mL of toluene. The mixture was kept under stirring under nitrogen at 60 °C for 2 h. The resultant PEGylated QDs were precipitated by 150 mL of ether, and then collected by centrifugation. After decanting the supernatant, 20 mL of Milli-Q water was introduced to redisperse the particles. The particle solution was subsequently purified by ultrafiltration at 5000 g using a 30 KD centrifugal filtration device (Millipore). The condensed solution was then ready for further experiments.

2.7. Cytotoxicity assay of PEGylated $CuInS_2$@ZnS:Mn QDs

The colorimetric MTT assay was performed to assess the cytotoxicity of the PEGylated $CuInS_2$@ZnS:Mn QDs for comparing with that of CdTe QDs. Specifically,

HeLa cells were first seeded in 96-well plates at a density of 4000 cells per well and cultured for about 24 h in DMEM supplemented with 10% FBS. Then, the cells were washed with 1× PBS and incubated with $CuInS_2$@ZnS:Mn QDs or CdTe QDs at different concentrations at 37 °C for 24 h. Subsequently, the cells were washed twice with 1× PBS followed by further proliferating in the culture medium for 48 h. Afterwards, 20 μL of MTT with a concentration of 5 mg/mL was added and allowed to react with the cells for 4 h before the addition of 150 μL of DMSO for dissolving of the precipitation. Finally, the absorption of each solution was measured at 490 nm on a microplate reader (Thermo, Varioskan Flash).

2.8. Animal tumor model

The tumor models used were established upon subcutaneous and intraperitoneal injection of LS180 cells ($\sim 5 \times 10^6$) into male BALB/c nude mice (4–6 weeks old) at the flank region of the right hind leg or the enterocoelia region. The tumor imaging studies were carried out 10 days after the inoculations of tumor cells.

2.9. MR imaging of tumors in vivo

A nude mouse bearing intraperitoneal tumor was anesthetized by 1% isoflurane delivered via a nose cone, and then via the tail vein the PEGylated $CuInS_2$@ZnS:Mn QDs were injected. The dose level was set to 5 μmol of Mn (or 0.4 μmol of QD nanoparticles) per kilogram body weight for PEGylated QDs. MR imaging was conducted on the Bruker Biospec animal MRI instrument (4.7 T, 30 cm) using a saturation-recovery spin-echo imaging sequence. The detailed imaging parameters were set as follows: field of view (FOV) = 3.5 × 4.5 cm^2; matrix size = 128 × 128; slice thickness = 1 mm; echo time (TE) = 11 ms; repetition time (TR) = 90, 150, 300, 500, 800, 1200, 2000, and 3000 ms; number of excitations (NEX) = 4. T_1 maps were calculated by pixel-wise fitting of the TR-dependent signal intensity changes to a single exponential function.

2.10. Fluorescence imaging of tumors in vivo

The fluorescence images of a nude mouse bearing subcutaneous tumor at the flank region of the right hind leg were acquired with a Maestro *in vivo* spectrum imaging system (Cambridge Research & Instrumentation, Woburn, MA). The dosage level was set the same as that for MRI experiments. The excitation filter was a narrow band filter to allow lights with wavelength of 503–548 nm to pass through; the emission filter was a 560 nm long-pass filter. The exposure time for acquiring each fluorescence image was set as 300 ms. The Maestro optical system consists of an optical head that includes a liquid crystal tunable filter (LCTF, with a bandwidth of 20 nm and a scanning wavelength range of 500–950 nm) with a custom-designed, spectrally optimized lens system that relays the image to a scientific-grade megapixel CCD. The CCD captured the images at each wavelength. The captured images can be analyzed by the vendor software, which uses spectral unmixing algorithms to separate autofluorescence from quantum dot signals [54]. The *ex vivo* fluorescence imaging of organs were performed similarly with the Maestro system.

All animal experiments reported herein were carried out according to a protocol approved by Peking University Institutional Animal Care and Use Committee.

2.11. Characterization

Fluorescence emission and fluorescence excitation spectra were recorded at room temperature on a Cary Eclipse fluorescence spectrophotometer; UV–Vis absorption spectra on a Cary 50 UV–Vis spectrophotometer. Low-resolution transmission electron microscopy (TEM) images and selected-area electron diffraction (SAED) patterns were recorded with a JEM-100CXII electron microscope operating at an accelerating voltage of 100 kV. High-resolution TEM (HRTEM) images were taken on FEI Tecnai20 and JEM-2100F microscopes working at an accelerating voltage of 200 kV. The metal composition and QD concentration were determined by the Inductively Coupled Plasma Optical Emission Spectrometer (ICP-OES) method using a Thermo Fisher IRIS Intrepid II XSP. Powder X-ray diffraction (XRD) patterns were obtained with a Regaku D/Max-2500 diffractometer equipped with a Cu $K\alpha_1$ radiation (λ = 1.54056 Å). The electron spin resonance (ESR) spectra were recorded on a Bruker ESP300 at room temperature. Longitudinal relaxation times were measured at 1.5 T (60 MHz) and 37 °C on a Bruker mq60 NMR analyzer.

3. Results and discussion

In brief, the $CuInS_2$ QDs were prepared by pyrolyzing indium(III) acetate at 200 °C in the presence of copper(I) iodide in 1-dodecanethiol (DDT). DDT served in the system as sulfur precursor and particle surface capping agent apart from a high boiling point solvent. After the $CuInS_2$ was formed, Zn stearate was introduced in the reaction system at room temperature and then the reaction system was heated up to 230 °C to facilitate the formation of ZnS shell. Thereafter, Mn(II) stearate in DDT was introduced dropwise after the reaction temperature was lowered to 180 °C for forming the doped particles through prolonged reaction time.

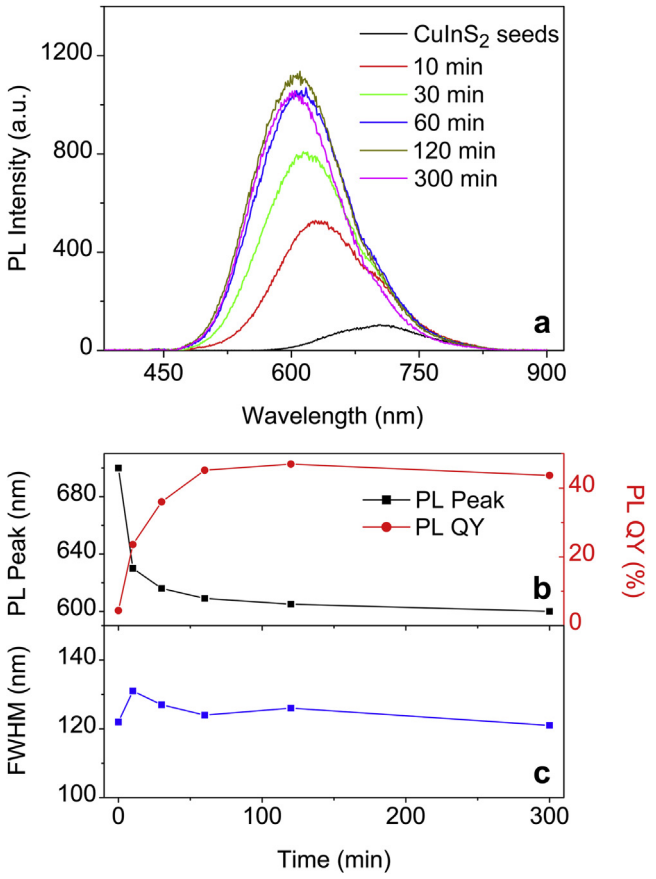

Fig. 1. a, Photoluminescence spectra of $CuInS_2$ seeds recorded during the ZnS coating process. b, Temporal evolutions of the PL peak position and PL QY against reaction time. c, Temporal evolution of FWHM against the reaction time. The excitation wavelength was 350 nm.

3.1. The impacts of ZnS coating on the optical properties of $CuInS_2$ QDs

As shown in Fig. 1a, 10 min of coating reaction leads to a remarkable blue shift of the PL emission peak from 709 nm to 632 nm (in the web version), leaving the emission of $CuInS_2$ as a shoulder. As a matter of fact, the chalcopyrite structure of $CuInS_2$ is a slightly modified form of zinc blende, in which Cu^+ and In^{3+} ions occupy the positions of Zn^{2+} ions. Due to the small difference between the ionic radii of Zn^{2+} and Cu^+ ions, Zn^{2+} ions are readily to diffuse into the $CuInS_2$ lattice [42,55,56]. Therefore, the initial strong blue shift of the PL peak can be attributed to the indiffusion of Zn^{2+}, consequently the radiative transition of the conduction band involving Zn^{2+} to internal defect levels occurs [47,57,58].

As shown in Fig. 1b, when the coating reaction is prolonged to 30 min, the emission peak position further shifts to the blue but by a reduced degree. In the meantime, the FWHM (full width at half maximum) of PL emission starts to decrease following the strong increase presented during the first 10 min, as shown in Fig. 1c, suggesting that an annealing process of the $CuInS_2$ incorporated with Zn^{2+} ions occurs. Thereafter, the variations of the blue shift and FWHM become no more evident, but the PL intensity can still be increased and eventually reach a maximum fluorescence QY of 47% at 120 min, which is in consistent with the experimental

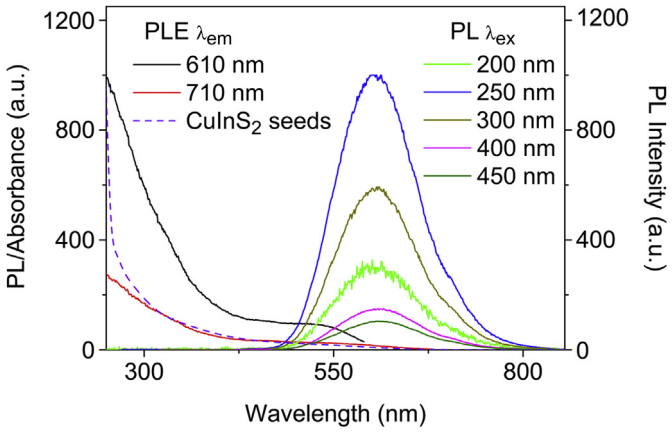

Fig. 2. Photoluminescence spectra of $CuInS_2$@ZnS QDs, obtained by reaction time of 120 min for ZnS coating, recorded by different excitation wavelengths, and photoluminescence excitation spectra recorded at different emission wavelengths. The purple dashed line is an absorption spectrum of original $CuInS_2$ seeds. (For interpretation of the references to color in this figure legend, the reader is referred to the web version of this article.)

observations previously published on coating Zn-Cu-In-S core with ZnS shell and therefore strongly suggests that the late stage of reaction is dominated by ZnS coating process rather than Zn^{2+} indiffusion [55,56].

In this context, the coating process can roughly be divided into three stages. Indiffusion of Zn^{2+} ions dominates the first stage, i.e., before 10 min, and ZnS coating dominates the last stage, i.e., after 30 min, while the indiffusion of Zn^{2+} ions, the annealing of the resultant Zn gradient core, and the surface ZnS coating coexist during the second stage, i.e., 10–30 min, which find supports from the evolution of the FWHM of the PL emission as shown in Fig. 1c. Further prolonging the reaction time to 300 min, the emission component of $CuInS_2$ with the peak position locating at around 709 nm keeps decreasing, implying that the annealing process for the $CuInS_2$ core with Zn gradient structure remains continuing.

To further confirm the structure of the cores involving Zn^{2+}, the optical properties of the nanoparticles with the highest fluorescence QY were subjected to further investigations. As shown in Fig. 2, the PL emission remains unchanged with respect to the peak position and FWHM upon excitation by incident lights of 200, 250, 300, 400, and 450 nm, respectively, which indicates that there is only one type of emissive center in the particles without any significant fraction of repetition nucleation occurring for ZnS. However, the PL excitation (PLE) spectrum monitored at PL emission of 610 nm strongly shifts to blue in comparison with that detected at 710 nm. Moreover, the latter highly resembles the absorption spectrum of the $CuInS_2$ seeds. Therefore, it can be concluded that the $CuInS_2$ cores remain but with a Zn gradient surface structure.

To further confirm the presence of the outer ZnS shell structure, the fluorescence lifetime measurements were carried out on the sample mentioned above. The PL decay curves are provided in Fig. S1 in the Supplementary Data. In general, the PL relaxations of the $CuInS_2$ seeds and $CuInS_2$@ZnS QDs were characterized by multi-exponential processes that were best fitted by three-exponential decays as summarized in Table 1. The entire recombination process of the initial $CuInS_2$ core particles was comprised of three decay components with time constants of 24 ns, 160 ns, and 501 ns, which according to literatures could be attributed to the surface defect related recombination (process 1), conduction band to internal defect recombination (process 2), and donor-acceptor pair recombination process (process 3), respectively [45,47,57,58]. The fitted results suggest that the former two radiative recombination

Table 1
The parameters, i.e., τ_i (time constant), B_i (amplitude) and their normalized products $\tau_iB_i/\Sigma\tau_iB_i$, for fitting the PL decay curves of different QDs by using three-exponential function. The lifetime-amplitude products represent the relative time-integrated contribution of each respective process to the overall number of emitted photons (i.e. the emission intensity measured in steady state PL spectra).

Sample	τ_1 (ns)	B_1 (%)	$\tau_1B_1/\Sigma\tau_iB_i$ (%)	τ_2 (ns)	B_2 (%)	$\tau_2B_2/\Sigma\tau_iB_i$ (%)	τ_3 (ns)	B_3 (%)	$\tau_3B_3/\Sigma\tau_iB_i$ (%)
$CuInS_2$	24	49	8	160	36	40	501	15	52
$CuInS_2$@ZnS	55	34	9	241	57	64	659	9	28
$CuInS_2$@ZnS:Mn	32	43	7	219	48	56	781	9	37

channels dominate the emission of $CuInS_2$ QDs (in terms of the relative amplitudes of their decay processes) at the PL peak position, with component amplitudes of 49% and 36%, respectively. In consequence of the ZnS coating process, the surface defect related recombination is obviously suppressed with its component amplitude decreasing to 34%, whilst the conduction band to internal defect relaxation is enhanced with the component amplitude increasing to 57%. The lifetime associated with the fast defect related channel increases from 24 ns to 55 ns indicating a reduction in the recombination rate via this channel and so the fast component contribution remains almost constant, going from 8% to 9% of the overall emitted fluorescence. A more significant impact of the addition of the ZnS layer though is seen in the changes to the second term in the decay process, associated with the conduction band to internal defect recombination process. Here the emission linked to this process increases in amplitude and lifetime, resulting in a net increase in emission from 40% of the signal to 64%, whilst in relative terms process 3 (donor-acceptor related recombination) diminishes in significance. The increase in the relative emission from process 2 is seen as evidence of the ready diffusion of Zn into the core, filling defects (e.g. vacancies) and thereby healing them. In absolute terms these relative changes give rise to an overall improvement in the QY of just over 10×, i.e. from a core QD QY of around 4% to a core/shell QD with lowered defect levels having a QY of around 47%. All these variations support the presence of an outer ZnS shell structure proposed above, with some indiffusion of Zn into the core. Even though the $CuInS_2$ core therefore most likely possesses a Zn gradient structure, in the following discussion, the current particle sample is denoted as $CuInS_2$@ZnS.

3.2. *The impacts of Mn-doping on the optical properties of $CuInS_2$@ZnS QDs*

To obtain fluorescence/MR dual-modality imaging probes based on the QDs mentioned above, properly balancing the Mn dopant concentration and the optical properties associated with the thickness of ZnS shell is essentially required for achieving molecular probes simultaneously visualizable through MRI and fluorescence imaging. Nevertheless, the Mn-doping of nanoparticles is often accompanied by decreases in the fluorescence QY of the host QDs [59,60]. Therefore, the fluorescence of $CuInS_2$@ZnS was monitored during the Mn-doping process.

In general the variation of PL can roughly be divided into two distinct stages bordered by 120 min, as shown in Fig. 3. The first stage of Mn-doping reaction slightly shifts the PL peak to the blue by curtailing the long-wavelength wing of the PL emission, and the PL emission peak position remains nearly unchanged but showing a progressively decreased intensity against reaction time (in the web version). Eventually the fluorescence QY is decreased to 35% by reaction time of 120 min. In contrast, the second stage (i.e., 120–300 min) of reaction strongly decreases the PL intensity and in the meantime shifts the PL emission peak from 600 nm to 620 nm. Therefore, it can be deduced that the structural annealing process

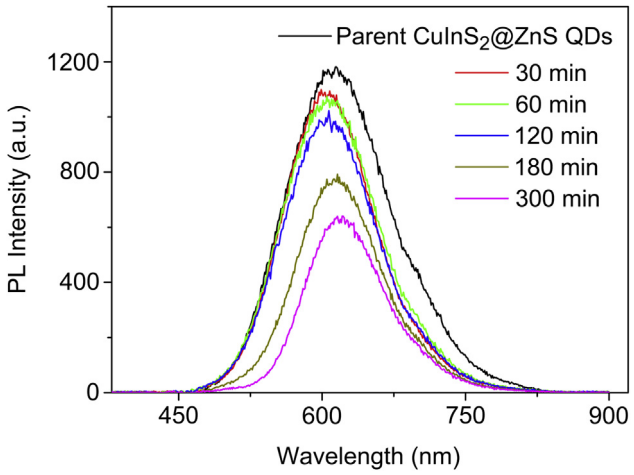

Fig. 3. Photoluminescence spectra of the $CuInS_2$@ZnS QDs recorded during the Mn-doping process. The excitation wavelength was 350 nm.

for the $CuInS_2$ with Zn gradient remains during the early stage of the reaction, which mainly suppresses the emission of $CuInS_2$ leaving the emission involving Zn^{2+} dominant. Moreover, the indiffusion of Mn^{2+} occurs presumably in the ZnS shell. In contrast, the deeper indiffusion of Mn^{2+} especially when the Mn^{2+} ion touches the emissive core, the fluorescence quenching effect takes place and in the meantime the PL peak is red-shifted, which can be explained by the interaction between the 3d electrons of Mn^{2+} and conduction/valence carriers [61]. The red-shift of PL could be resulted from two perturbations from Mn dopants: firstly, the newly appeared *p-d* hybridization between Mn 3d electrons and the anion-*p* states is expected to elevate the valence band, which could be conceivable to give rise to the narrowing of the band gap, consequently resulting the red-shifts [61]; secondly, the hole may be traped in Mn-related intraband defect states, and thus this intraband trap state emits [59,62]. According to these analyses, the red-shift of PL can be taken as an indication for successful Mn-doping. Therefore, the sample obtained by 180 min was used in the following experiments, and denoted as $CuInS_2$@ZnS:Mn because the fluorescence QY of the resultant particles remains relatively high (27.2%). In comparison with $CuInS_2$@ZnS QDs, as shown in Table 1, the $CuInS_2$@ZnS:Mn QDs present an increased component amplitude for surface defect related recombination accompanied by a compensating reduction in lifetime (increase in recombination rate), and a decreased component amplitude for the conduction band to internal defect recombination, which also support that Mn^{2+} ions have successfully been doped in the $CuInS_2$@ZnS QDs. In terms of the relative contributions of the three processes, the uptake of Mn^{2+} ions partially reverses the effect of the ZnS shell addition in the first stage – the contribution of the surface defect related process to the overall steady state fluorescence remains more or less constant (9% dropping to 7%) due to the compensating changes in lifetime and amplitude, but the drop in both lifetime and decay amplitude of the conduction band to internal defect related recombination process reduces that contribution to the emitted fluorescence (56% from 64%), making the donor-acceptor contribution (37%) correspondingly more significant than in the un-doped case (28%). Again this supports the onset of greater intrusion of Mn^{2+} into the core by reaction time of 180 min.

To further disclose the impact of dopant concentration of Mn^{2+} on the optical properties of the host particles, the sample obtained by 180 min of the doping reaction was named as sample A for comparing with two additional samples, i.e., sample B and sample C. Sample B was obtained by increasing the feeding amount of Mn precursor by a factor of 2.5, while sample C was obtained simultaneously decreasing the feeding amounts of Zn and Mn precursors by a factor of 2.5. The metal contents of samples A–C based on ICP-OES measurements are provided in Table 2. In comparison with sample A, the Mn content in sample B is doubled while the Zn content remains nearly unchanged with reference to In. In consequence of the increased Mn concentration, sample B present a sharp decrease in fluorescence QY down to 13.2% from 27.2% for sample A. Furthermore, the PL emission of the reaction system for obtaining sample B was largely shifted to red in comparison with former system for preparing sample A over the whole reaction process as shown in Fig. S2, which supports that the red-shift of PL can be taken as an indicator for successful Mn-doping. Decreasing the feeding amount of Zn precursor dramatically leads to a reduced Zn content with reference to In, consequently resulting in a thinner ZnS shell for $CuInS_2$@ZnS QDs. By properly controlling the reaction time for Mn-doping, sample C showing the same Mn-doping level as sample A was obtained. But sample C is also characterized by largely reduced fluorescence QY, demonstrating that the ZnS shell can effectively protect the core particle from fluorescence quenching upon Mn-doping.

Table 2
The molar ratios of Mn:In and Zn:In determined from ICP-OES analysis for samples A–C together with the corresponding fluorescence QY.

Sample	Mn:In	Zn:In	QY (%)
A	0.08	5.79	27.2
B	0.20	5.60	13.2
C	0.09	2.39	16.4

3.3. Morphology and phase structure of $CuInS_2$@ZnS and $CuInS_2$@ZnS:Mn QDs

Representative transmission electron microscopy (TEM) and high-resolution TEM (HRTEM) images extracted from large area images (Fig. S3 of Supplementary Data) of the $CuInS_2$ seeds, $CuInS_2$@ZnS, and $CuInS_2$@ZnS:Mn (sample A) QDs together with their particle size distribution profiles are shown in Fig. 4. The average diameter of the $CuInS_2$ seeds is increased from 2.9 ± 0.5 nm to 3.6 ± 0.5 nm upon ZnS coating, which supports for formation of outer ZnS shell. The Mn-doping process hardly changes the particle size and the average diameter of the particles in sample A is of 3.6 ± 0.6 nm. Given the thickness of 0.312 nm for one monolayer ZnS [24,63,64], the average thickness of the ZnS shell for $CuInS_2$@ZnS QDs and $CuInS_2$@ZnS:Mn QDs is thus estimated to be around 1.1 monolayers of ZnS. The HRTEM measurements together with electron diffraction patterns of these three particle samples further indicate that the doping and the following Mn-doping processes did not alter the chalcopyrite structure of the $CuInS_2$ seeds. Nevertheless, the ZnS coating gives rise to slight shifts to the diffraction peaks to high scattering angles according to X-ray diffraction results shown in Fig. S4 in Supplementary Data.

3.4. Magnetic properties of $CuInS_2$@ZnS:Mn QDs

Electron spin resonance (ESR) measurements were performed to further investigate the magnetic properties of $CuInS_2$@ZnS:Mn QDs. All the samples for ESR measurements were extensively purified by three cycles of precipitation of QDs with acetone, centrifugation, and redissolution in cyclohexane. A representative single line ESR spectrum with a broad peak is recorded from sample A as presented in Fig. S5. The observed ESR signals are proposed to be originated from the manganese chemically bonded rather than any

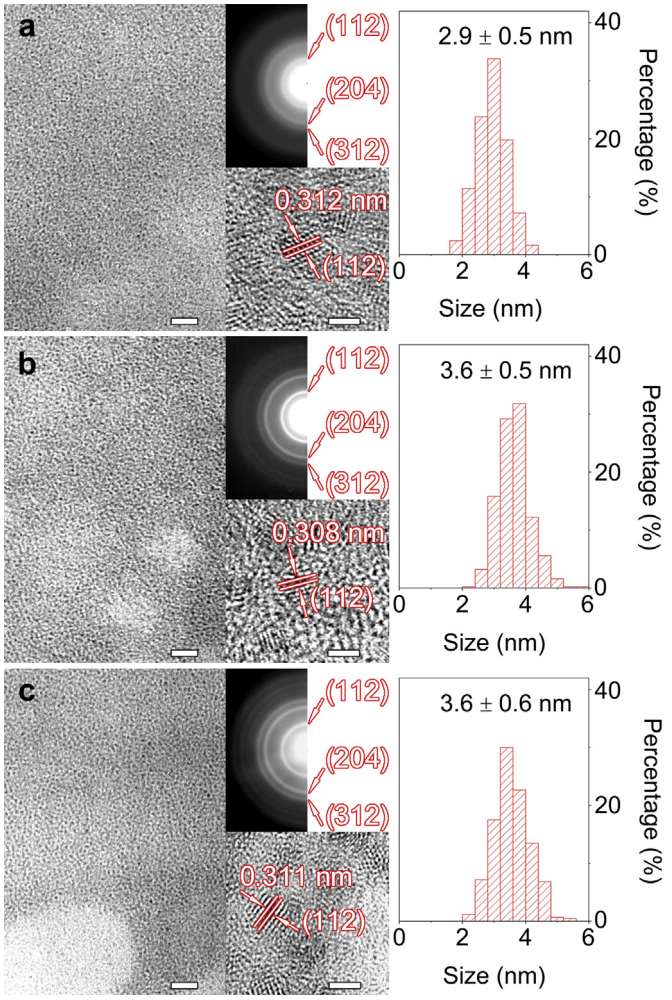

Fig. 4. TEM and high resolution TEM images of $CuInS_2$ QDs (a), $CuInS_2$@ZnS QDs (b), and $CuInS_2$@ZnS:Mn QDs (c), together with corresponding selected area electron diffraction (SAED) patterns and particle size histograms. The scale bars in the TEM and HRTEM correspond to 20 nm and 2 nm, respectively.

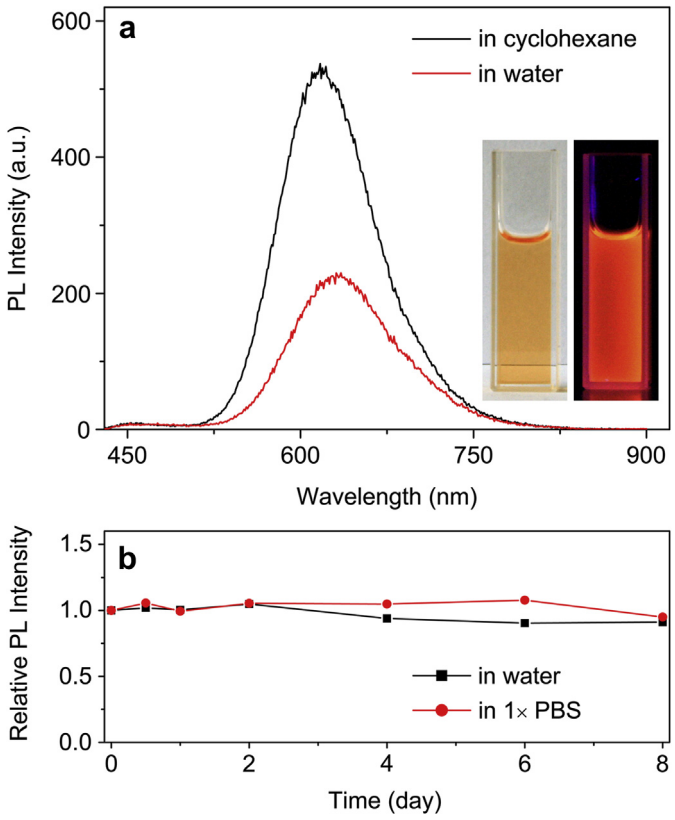

Fig. 5. a, Photoluminescence spectra of sample A (in cyclohexane) and the PEGylated sample A (in water), the insets are photographs of an aqueous solution of the PEGylated sample A captured under ambient light (left) and UV light (right). b, Temporal behaviors of the photoluminescence intensity of the PEGylated $CuInS_2$@ZnS:Mn QDs in water and 1× PBS.

remnants of free manganese loosely absorbed on the surface of $CuInS_2$@ZnS:Mn, because the manganese doping levels determined from ICP-OES results (Table S1 of Supplementary Data) before and after surface ligand exchange and further extensive purification by centrifugal filtration as outlined in the Materials and methods Section 2.6 kept unchanged. The absence of hyperfine splitting structure is probably caused by spin–spin interactions between Mn^{2+} ions close to each other [29,32,65,66]. More importantly, the structural defects such as vacancies and their induced anti-site defects are readily formed in the $CuInS_2$ host. These defect centers are considered to bring additional random perturbations to electron-nuclear hyperfine coupling of Mn^{2+} [66], consequently leading to a net inhomogeneous broadening by masking the hyperfine splitting structure.

In comparison with sample A, samples B and C exhibited the same ESR features. But the signal intensity of sample B was increased by a factor of 2.4, while the signal intensity of sample C was rather comparable, in comparison with that of sample A.

3.5. PEGylated $CuInS_2$@ZnS:Mn QDs

With respect to applications in tumor imaging, water solubility and colloidal stability are essentially required for the aforementioned $CuInS_2$@ZnS:Mn QDs. Therefore, a poly(ethylene glycol)-based hydrophilic ligand bearing a dithiol moiety was designed and used for replacing the native hydrophobic ligands of the bifunctional particles.

Upon ligand exchange, the fluorescence QY of the $CuInS_2$@ZnS:Mn QDs (sample A) drops by approximately 54%, accompanied by a red shift of 18 nm with respect to the PL peak position (in the web version). Nonetheless, the resultant nanoparticles remain highly fluorescent in water as shown in the inset of Fig. 5a. Most importantly the aqueous solution is very well transparent, suggesting that the resultant particles possess excellent dispersibility in aqueous system. Long-term (till 8 days) observations further demonstrate that the PEG-coated $CuInS_2$@ZnS:Mn QDs present very stable PL emission, as shown in Fig. 5b, which further suggests that the resultant particles also possess long-term colloidal stability in both water and PBS buffer.

3.6. R_1 relaxivity of PEGylated $CuInS_2$@ZnS:Mn QDs

The performance of the PEGylated $CuInS_2$@ZnS:Mn QDs as MRI contrast agents was evaluated on a 1.5 T NMR analyzer. As shown in Fig. 6a, the experimentally determined longitudinal relaxation rates R_1 of water protons was plotted against the molar concentration of Mn. Derived from the slopes of the concentration dependent R_1, the concentration-independent relaxivity (r_1) was extracted as 5.84 ± 0.26 mM^{-1} s^{-1}, 4.47 ± 0.06 mM^{-1} s^{-1}, and 6.34 ± 0.50 mM^{-1} s^{-1} for PEGylated samples A–C, respectively. In comparison with sample A, sample B present a reduced r_1, which is probably caused by enhanced spin–spin interactions between

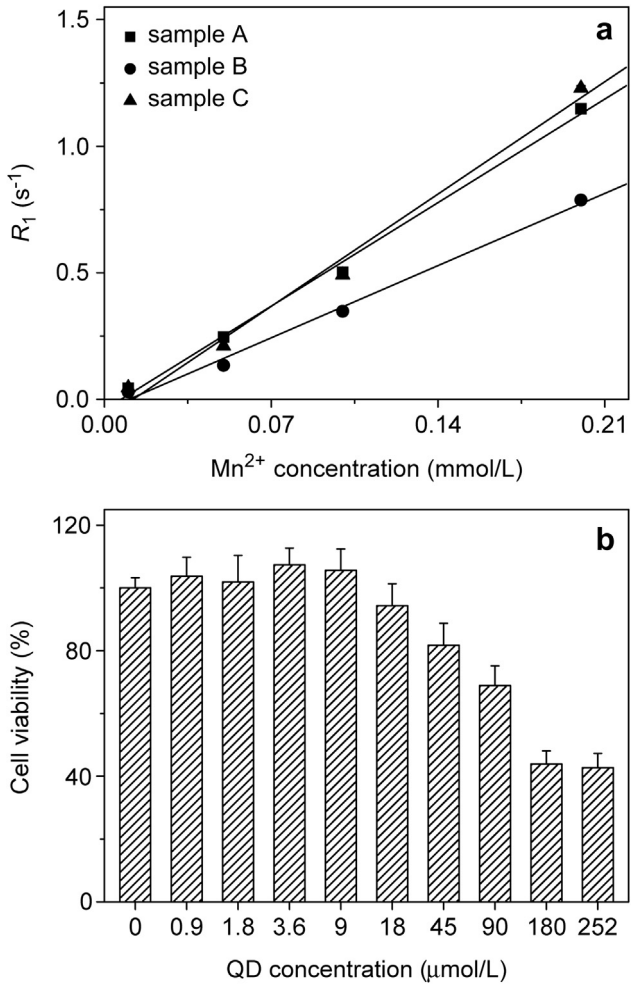

Fig. 6. a, Longitudinal relaxation rate (R_1) (solid symbol) against the concentration of Mn^{2+} ions for samples A–C, overlaid with the corresponding linear fits (solid line). b, Cell viability of HeLa cells recorded after being incubated with PEGylated sample A.

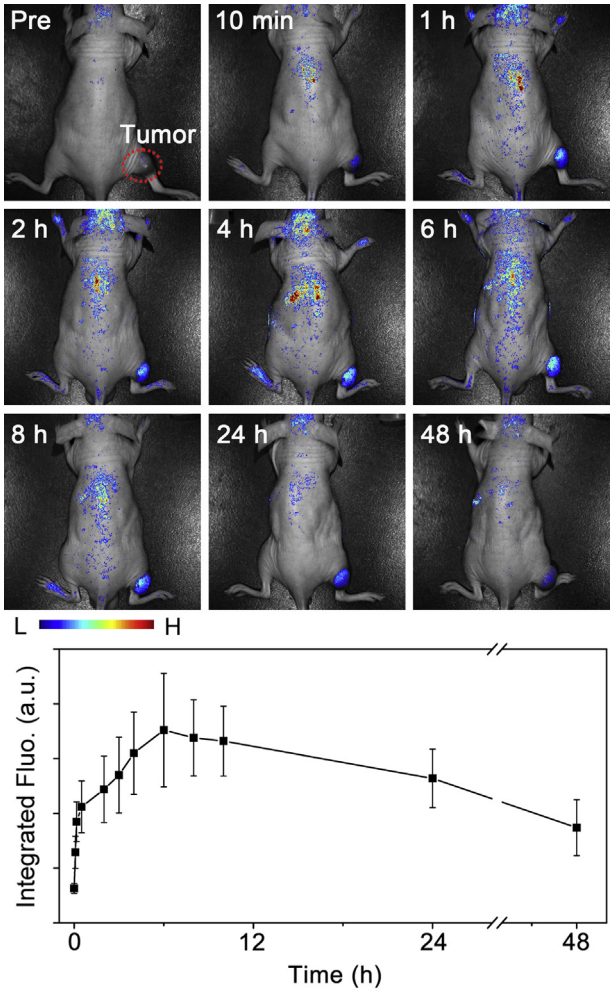

Fig. 7. Upper frame: *in vivo* fluorescence imaging of the nude mouse bearing a subcutaneous tumor, as indicated by the red dashed line circle, recorded pre- and at different time points post-injection of the PEGylated sample A. Lower frame: temporal evolutions of the integrated fluorescence signals recorded from the tumor region.

Mn^{2+} ions due to its higher Mn^{2+} dopant concentration. While the slightly increased r_1 value for sample C is probably caused by enhanced tumbling rate of the $CuInS_2$@ZnS:Mn particle with slightly reduced ZnS shell thickness [67,68]. By taking the overall fluorescent and magnetic properties of samples A–C, sample A was chosen for the following bioapplication experiments.

3.7. Cytotoxicity of PEGylated $CuInS_2$@ZnS:Mn QDs

Before further *in vivo* experiments, the cytotoxicity of the PEGylated $CuInS_2$@ZnS:Mn QDs was evaluated through MTT assays on the proliferation of HeLa cells. As is shown in Fig. 6b, below 9 μmol/L the PEGylated $CuInS_2$@ZnS:Mn QDs present nearly no toxicity to HeLa cells. The cell viability starts to decrease when the particle concentration is higher than 45 μmol/L, but remains above 40% even when the particle concentration reaches 252 μmol/L. Further theoretical fitting demonstrates that the IC_{50} (50% inhibitory concentration) value of the PEGylated $CuInS_2$@ZnS:Mn QDs is about 167.9 ± 9.9 μmol/L, in huge contrast to 0.023 ± 0.002 μmol/L for thioglycolic acid stabilized CdTe QDs synthesized according to literature [69–71], according to the results shown in Fig. S6 in Supplementary Data. This huge difference clearly manifests the suitability of the Cd-free $CuInS_2$@ZnS:Mn QDs for *in vivo* applications in comparison with the cadmium chalcogenide QDs. Since the chosen QD dose for the PEGylated $CuInS_2$@ZnS:Mn QDs was set to 0.4 μmol/kg body weight, it is reasonable to believe that the current PEGylated QDs present extremely low cytotoxicity for being used as fluorescence and MR imaging probes.

3.8. Fluorescence and MR dual-modality imaging of tumors in vivo

To show the potential of the current bifunctional particles in tumor imaging, passive tumor targeting mechanism based on enhanced permeability and retention (EPR) effect was adopted [72–74]. Through tail vein the PEGylated sample A was intravenously injected into BALB/c nude mice subcutaneously transplanted with LS180 tumor cells at the flank region of the right hind leg or the enterocoelia region.

A set of fluorescence images acquired pre- and at different time points post-injection are presented in Fig. 7. The quantified fluorescence signals recorded from tumor region are shown in Fig. 7. It can be seen that a significant fluorescence signal appears at 10 min post-injection from the tumor region and then quickly increases to a maximum at around 6 h. In the meantime, some signals from back position appear possibly from nonspecific signals caused by the variations of skin temperature and humidity, considering that the changes of signal position against time was not fixed. But these

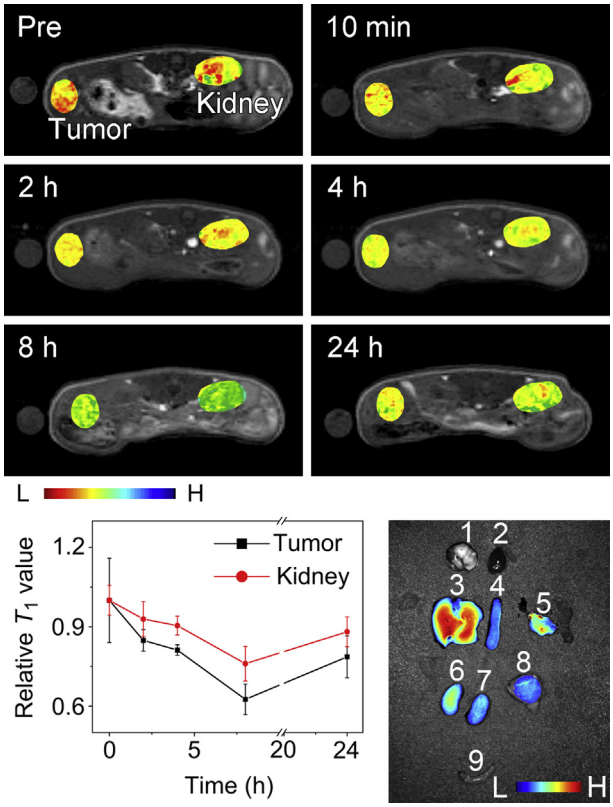

Fig. 8. Upper panel: T_1-weighted MR images acquired pre- and at different time points after intravenous injection of the PEGylated $CuInS_2$@ZnS:Mn QDs into the mouse bearing intraperitoneally transplanted tumors, both the tumor and kidney are color-coded for better showing the contrast enhancing effects. Left frame of the lower panel: temporal T_1 values of tumor and kidney sites. Right frame of the lower panel: *ex vivo* fluorescence images of main organs harvested 24 h postinjection: 1, lung; 2, heart; 3, liver; 4, spleen; 5, part of stomach; 6, kidney (left); 7, kidney (right); 8, tumor; 9, part of intestine.

background signals decay by the same tendency as that from the tumor region and eventually become rather weak at 48 h post-injection.

In comparison with the subcutaneous tumor model, the intraperitoneally transplanted tumor can better reflect the nature of cancers as it can be taken as a metastatic model. In the following experiments, *in vivo* MR study was performed on the nude mice bearing tumor xenografts implanted at their enterocoelia regions. T_1-weighted MR images acquired before and at different time points after intravenous injections of PEGylated sample A are shown in the upper panel of Fig. 8. The dosage level was set the same as that for fluorescence imaging. In general, the T_1 value of the tumor region starts to decrease and reaches a minimum at 8 h post-injection. In the meantime, kidney also presents a similar variation in T_1 value, as shown in the left frame in the lower panel of Fig. 8, suggesting that renal clearance may be the possible elimination pathway for the current particles due to their small particle size [75]. In addition, liver also presents similar temporal T_1 value as shown in Fig. S7.

To further show the biodistribution of the injected particles, the main organs such as lung, heart, liver, spleen, part of stomach, kidney, tumor, and part of intestine were collected at 24 h post-injection and subjected to fluorescence imaging measurements. The imaging results are shown in the right frame in the lower panel of Fig. 8. In general, liver presents the strongest signal, followed by stomach, kidney, tumor, and spleen, but no optical signal can be observed from heart and lung. As one of the normal functions of liver and spleen from the reticuloendothelial system is to purify blood of foreign particles, therefore they present certain uptakes of the injected particles. The strong signals from kidney further suggest that some of the injected particles are excreted through the renal clearance pathway. Although the T_1 contrast effect becomes very weak at 24 h post-injection, the fluorescence imaging results suggest that there remains a detectable optical signal from the tumor harvested. With respect to the fluorescence signal from stomach, careful experimental observation revealed that it was actually from the food residues in the stomach.

4. Conclusions

In summary, we have successfully synthesized a new type of Mn-doped Cd-free QDs with Zn gradient $CuInS_2$ core and ZnS outer shell. Systematic studies reveal that the ZnS shell on the one hand can enhance the fluorescence of the underlying core, and on the other hand prevent the core particle from heavy fluorescence quenching caused by Mn-doping in achieving highly fluorescent Mn-doped QDs. The PEGylated $CuInS_2$@ZnS:Mn QDs obtained through ligand exchange process by using DHLA-PEG ligand present 7000 times lower cytotoxicity to HeLa cells than CdTe QDs, apart from excellent optical properties and colloidal stabilities in water and PBS buffer, which makes the current magnetic dots an excellent choice for further *in vivo* applications. The preliminary experiments on fluorescence and MR imaging of tumors have shown that the both subcutaneous and intraperitoneal tumor xenografts can be visualized *in vivo*. We therefore believe that our current synthetic protocol may pave a reliable way for constructing high performance imaging probes with greatly reduced toxicity for versatile *in vivo* applications.

Acknowledgments

The authors thank the National Basic Research Program of China (2011CB935800), the National Nature Science Foundation of China (21203210, 81090271, 21021003, 21003135), Institute of Chemistry, CAS (CMS-PY-201321, CMS-PY-201309) for financial support. The authors are grateful to Prof. Hao Lei, and Dr. Meihong Du for their kind help with respect to MRI and relaxivity experiments. The authors are also grateful to Prof. Alexander Eychmüller from TU Dresden for his kind discussion.

Appendix A. Supplementary data

Supplementary data related to this article can be found online at http://dx.doi.org/10.1016/j.biomaterials.2013.10.078.

References

[1] Louie AY. Multimodality imaging probes: design and challenges. Chem Rev 2010;110:3146–95.
[2] Koole R, Mulder WJM, van Schooneveld MM, Strijkers GJ, Meijerink A, Nicolay K. Magnetic quantum dots for multimodal imaging. Wiley Interdiscip Rev-Nanomed Nanobiotechnol 2009;1:475–91.
[3] Lee DE, Koo H, Sun IC, Ryu JH, Kim K, Kwon IC. Multifunctional nanoparticles for multimodal imaging and theragnosis. Chem Soc Rev 2012;41:2656–72.
[4] Zrazhevskiy P, Sena M, Gao XH. Designing multifunctional quantum dots for bioimaging, detection, and drug delivery. Chem Soc Rev 2010;39:4326–54.
[5] Chen C, Peng J, Sun SR, Peng CW, Li Y, Pang DW. Tapping the potential of quantum dots for personalized oncology: current status and future perspectives. Nanomedicine 2012;7:411–28.
[6] Tsukamoto E, Ochi S. PET/CT today: system and its impact on cancer diagnosis. Ann Nucl Med 2006;20:255–67.
[7] Cherry SR, Louie AY, Jacobs RE. The integration of positron emission tomography with magnetic resonance imaging. Proc IEEE 2008;96:416–38.

[8] Ntziachristos V, Ripoll J, Wang LV, Weissleder R. Looking and listening to light: the evolution of whole-body photonic imaging. Nat Biotechnol 2005;23:313–20.

[9] Lee JH, Jun YW, Yeon SI, Shin JS, Cheon J. Dual-mode nanoparticle probes for high-performance magnetic resonance and fluorescence imaging of neuroblastoma. Angew Chem Int Ed 2006;45:8160–2.

[10] Wu P, Yan XP. Doped quantum dots for chemo/biosensing and bioimaging. Chem Soc Rev 2013;42:5489–521.

[11] Gao J, Zhang B, Gao Y, Pan Y, Zhang X, Xu B. Fluorescent magnetic nanocrystals by sequential addition of reagents in a one-pot reaction: a simple preparation for multifunctional nanostructures. J Am Chem Soc 2007;129:11928–35.

[12] Kim H, Achermann M, Balet LP, Hollingsworth JA, Klimov VI. Synthesis and characterization of Co/CdSe core/shell nanocomposites: bifunctional magnetic-optical nanocrystals. J Am Chem Soc 2004;127:544–6.

[13] Kwon K-W, Shim M. γ-Fe_2O_3/II–VI sulfide nanocrystal heterojunctions. J Am Chem Soc 2005;127:10269–75.

[14] Kim J, Lee JE, Lee SH, Yu JH, Lee JH, Park TG, et al. Designed fabrication of a multifunctional polymer nanomedical platform for simultaneous cancer-targeted imaging and magnetically guided drug delivery. Adv Mater 2008;20:478–83.

[15] Park J-H, von Maltzahn G, Ruoslahti E, Bhatia SN, Sailor MJ. Micellar hybrid nanoparticles for simultaneous magnetofluorescent imaging and drug delivery. Angew Chem Int Ed 2008;120:7394–8.

[16] Zebli B, Susha AS, Sukhorukov GB, Rogach AL, Parak WJ. Magnetic targeting and cellular uptake of polymer microcapsules simultaneously functionalized with magnetic and luminescent nanocrystals. Langmuir 2005;21:4262–5.

[17] Cormode DP, Skajaa T, van Schooneveld MM, Koole R, Jarzyna P, Lobatto ME, et al. Nanocrystal core high-density lipoproteins: a multimodality contrast agent platform. Nano Lett 2008;8:3715–23.

[18] Mulder WJM, Castermans K, van Beijnum JR, Egbrink M, Chin PTK, Fayad ZA, et al. Molecular imaging of tumor angiogenesis using alpha v beta 3-integrin targeted multimodal quantum dots. Angiogenesis 2009;12:17–24.

[19] Prinzen L, Miserus R-JJHM, Dirksen A, Hackeng TM, Deckers N, Bitsch NJ, et al. Optical and magnetic resonance imaging of cell death and platelet activation using Annexin A5-functionalized quantum dots. Nano Lett 2006;7:93–100.

[20] Yang HS, Santra S, Walter GA, Holloway PH. Gd-III-functionalized fluorescent quantum dots as multimodal imaging probes. Adv Mater 2006;18:2890–4.

[21] Erwin SC, Zu LJ, Haftel MI, Efros AL, Kennedy TA, Norris DJ. Doping semiconductor nanocrystals. Nature 2005;436:91–4.

[22] Norris DJ, Efros AL, Erwin SC. Doped nanocrystals. Science 2008;319:1776–9.

[23] Santra S, Yang H, Holloway PH, Stanley JT, Mericle RA. Synthesis of water-dispersible fluorescent, radio-opaque, and paramagnetic CdS: Mn/ZnS quantum dots: A multifunctional probe for bioimaging. J Am Chem Soc 2005;127:1656–7.

[24] Wang S, Jarrett BR, Kauzlarich SM, Louie AY. Core/shell quantum dots with high relaxivity and photoluminescence for multimodality imaging. J Am Chem Soc 2007;129:3848–56.

[25] Mikulec FV, Kuno M, Bennati M, Hall DA, Griffin RG, Bawendi MG. Organometallic synthesis and spectroscopic characterization of manganese-doped CdSe nanocrystals. J Am Chem Soc 2000;122:2532–40.

[26] Yang YA, Chen O, Angerhofer A, Cao YC. Radial-position-controlled doping in CdS/ZnS core/shell nanocrystals. J Am Chem Soc 2006;128:12428–9.

[27] Santra S, Yang H, Stanley JT, Holloway PH, Moudgil BM, Walter G, et al. Rapid and effective labeling of brain tissue using TAT-conjugated CdS: Mn/ZnS quantum dots. Chem Commun 2005:3144–6.

[28] Pradhan N, Peng XG. Efficient and color-tunable Mn-doped ZnSe nanocrystal emitters: control of optical performance via greener synthetic chemistry. J Am Chem Soc 2007;129:3339–47.

[29] Gonzalez Beermann PA, McGarvey BR, Muralidharan S, Sung RCW. EPR spectra of Mn^{2+}-doped ZnS quantum dots. Chem Mater 2004;16:915–8.

[30] Nag A, Chakraborty S, Sarma DD. To dope Mn^{2+} in a semiconducting nanocrystal. J Am Chem Soc 2008;130:10605–11.

[31] Bhargava RN, Gallagher D, Hong X, Nurmikko A. Optical properties of manganese-doped nanocrystals of ZnS. Phys Rev Lett 1994;72:416–9.

[32] Biswas S, Kar S, Chaudhuri S. Optical and magnetic properties of manganese-incorporated zinc sulfide nanorods synthesized by a solvothermal process. J Phys Chem B 2005;109:17526–30.

[33] Derfus AM, Chan WCW, Bhatia SN. Probing the cytotoxicity of semiconductor quantum dots. Nano Lett 2004;4:11–8.

[34] Su YY, He Y, Lu HT, Sai LM, Li QN, Li WX, et al. The cytotoxicity of cadmium based, aqueous phase–synthesized, quantum dots and its modulation by surface coating. Biomaterials 2009;30:19–25.

[35] Rogach AL, Franzl T, Klar TA, Feldmann J, Gaponik N, Lesnyak V, et al. Aqueous synthesis of thiol-capped CdTe nanocrystals: state-of-the-art. J Phys Chem C 2007;111:14628–37.

[36] Qian H, Dong C, Weng J, Ren J. Facile one-pot synthesis of luminescent, water-soluble, and biocompatible glutathione-coated CdTe nanocrystals. Small 2006;2:747–51.

[37] Gaponik N, Talapin DV, Rogach AL, Hoppe K, Shevchenko EV, Kornowski A, et al. Thiol-capping of CdTe nanocrystals: an alternative to organometallic synthetic routes. J Phys Chem B 2002;106:7177–85.

[38] Wang SP, Mamedova N, Kotov NA, Chen W, Studer J. Antigen/antibody immunocomplex from CdTe nanoparticle bioconjugates. Nano Lett 2002;2:817–22.

[39] Gao XH, Cui YY, Levenson RM, Chung LWK, Nie SM. In vivo cancer targeting and imaging with semiconductor quantum dots. Nat Biotechnol 2004;22:969–76.

[40] Wu WT, Aiello M, Zhou T, Berliner A, Banerjee P, Zhou SQ. In-situ immobilization of quantum dots in polysaccharide-based nanogels for integration of optical pH-sensing, tumor cell imaging, and drug delivery. Biomaterials 2010;31:3023–31.

[41] Pons T, Pic E, Lequeux N, Cassette E, Bezdetnaya L, Guillemin F, et al. Cadmium-free $CuInS_2$/ZnS quantum dots for sentinel lymph node imaging with reduced toxicity. ACS Nano 2010;4:2531–8.

[42] Deng D, Chen Y, Cao J, Tian J, Qian Z, Achilefu S, et al. High-quality $CuInS_2$/ZnS quantum dots for in vitro and in vivo bioimaging. Chem Mater 2012;24:3029–37.

[43] Yong KT, Roy I, Hu R, Ding H, Cai HX, Zhu J, et al. Synthesis of ternary $CuInS_2$/ZnS quantum dot bioconjugates and their applications for targeted cancer bioimaging. Integr Biol 2010;2:121–9.

[44] Han W, Yi LX, Zhao N, Tang AW, Gao MY, Tang ZY. Synthesis and shape-tailoring of copper sulfide/indium sulfide-based nanocrystals. J Am Chem Soc 2008;130:13152–61.

[45] Li L, Daou TJ, Texier I, Chi T T Kim, Liem NQ, Reiss P. Highly luminescent $CuInS_2$/ZnS core/shell nanocrystals: cadmium-free quantum dots for in vivo imaging. Chem Mater 2009;21:2422–9.

[46] Xie RG, Rutherford M, Peng XG. Formation of high-quality I-III-VI semiconductor nanocrystals by tuning relative reactivity of cationic precursors. J Am Chem Soc 2009;131:5691–7.

[47] Li LA, Pandey A, Werder DJ, Khanal BP, Pietryga JM, Klimov VI. Efficient synthesis of highly luminescent copper indium sulfide-based core/shell nanocrystals with surprisingly long-lived emission. J Am Chem Soc 2011;133:1176–9.

[48] Castro SL, Bailey SG, Raffaelle RP, Banger KK, Hepp AF. Nanocrystalline chalcopyrite materials ($CuInS_2$ and $CuInSe_2$) via low-temperature pyrolysis of molecular single-source precursors. Chem Mater 2003;15:3142–7.

[49] Zhong HZ, Zhou Y, Ye MF, He YJ, Ye JP, He C, et al. Controlled synthesis and optical properties of colloidal ternary chalcogenide $CuInS_2$ nanocrystals. Chem Mater 2008;20:6434–43.

[50] Park J, Kim SW. $CuInS_2$/ZnS core/shell quantum dots by cation exchange and their blue-shifted photoluminescence. J Mater Chem 2011;21:3745–50.

[51] Hu FQ, Wei L, Zhou Z, Ran YL, Li Z, Gao MY. Preparation of biocompatible magnetite nanocrystals for in vivo magnetic resonance detection of cancer. Adv Mater 2006;18:2553–6.

[52] Liu SJ, Jia B, Qiao RR, Yang Z, Yu ZL, Liu ZF, et al. A novel type of dual-modality molecular probe for MR and nuclear imaging of tumor: preparation, characterization and in vivo application. Mol Pharmaceut 2009;6:1074–82.

[53] Hou Y, Qiao RR, Fang F, Wang XX, Dong CY, Liu K, et al. $NaGdF_4$ nanoparticle-based molecular probes for magnetic resonance imaging of intraperitoneal tumor xenografts in vivo. ACS Nano 2012;7:330–8.

[54] Levenson RM. Spectral imaging and pathology: seeing more. Lab Med 2004;35:244–52.

[55] Guo W, chen N, Tu Y, Dong C, Zhang B, Hu C, et al. Synthesis of Zn-Cu-In-S/ZnS core/shell quantum dots with inhibited blue-shift photoluminescence and applications for tumor targeted bioimaging. Theranostics 2013;3:99–108.

[56] Nam D-E, Song W-S, Yang H. Facile, air-insensitive solvothermal synthesis of emission-tunable $CuInS_2$/ZnS quantum dots with high quantum yields. J Mater Chem 2011;21:18220–6.

[57] Tran TKC, Le QP, Nguyen QL, Li L, Reiss P. Time-resolved photoluminescence study of $CuInS_2$/ZnS nanocrystals. Adv Nat Sci Nanosci Nanotechnol 2010;1:025007.

[58] Nose K, Omata T, Otsuka-Yao-Matsuo S. Colloidal synthesis of ternary copper indium diselenide quantum dots and their optical properties. J Phys Chem C 2009;113:3455–60.

[59] Beaulac R, Archer PI, Liu X, Lee S, Salley GM, Dobrowolska M, et al. Spin-polarizable excitonic luminescence in colloidal Mn^{2+}-doped CdSe quantum dots. Nano Lett 2008;8:1197–201.

[60] Bol AA, Meijerink A. Luminescence quantum efficiency of nanocrystalline ZnS: Mn^{2+}. 1. surface passivation and Mn^{2+} concentration. J Phys Chem B 2001;105:10197–202.

[61] Fleszar A, Potthoff M, Hanke W. Electronic structure of zinc-blende MnTe within the GW approximation. Phys Stat Sol (C) 2007;4:3270–9.

[62] Manna G, Jana S, Bose R, Pradhan N. Mn-doped multinary CIZS and AIZS nanocrystals. J Phys Chem Lett 2012;3:2528–34.

[63] Dabbousi BO, RodriguezViejo J, Mikulec FV, Heine JR, Mattoussi H, Ober R, et al. (CdSe)ZnS core-shell quantum dots: synthesis and characterization of a size series of highly luminescent nanocrystallites. J Phys Chem B 1997;101:9463–75.

[64] Peng XG, Schlamp MC, Kadavanich AV, Alivisatos AP. Epitaxial growth of highly luminescent CdSe/CdS core/shell nanocrystals with photostability and electronic accessibility. J Am Chem Soc 1997;119:7019–29.

[65] Schneider EE, England TS. Paramagnetic resonance at large magnetic dilutions. Physica 1951;17:221–33.

[66] Murase N, Jagannathan R, Kanematsu Y, Watanabe M, Kurita A, Hirata K, et al. Fluorescence and EPR characteristics of Mn^{2+}-doped ZnS nanocrystals prepared by aqueous colloidal method. J Phys Chem B 1999;103:754–60.

[67] Lauffer RB. Paramagnetic metal complexes as water proton relaxation agents for NMR Imaging: theory and design. Chem Rev 1987;87:901–27.

[68] Na HB, Lee JH, An KJ, Park YI, Park M, Lee IS, et al. Development of a T-1 contrast agent for magnetic resonance imaging using MnO nanoparticles. Angew Chem Int Ed 2007;46:5397–401.
[69] Gao MY, Kirstein S, Möhwald H, Rogach AL, Kornowski A, Eychmüller A, et al. Strongly photoluminescent CdTe nanocrystals by proper surface modification. J Phys Chem B 1998;102:8360–3.
[70] Jing LH, Yang CH, Qiao RR, Niu M, Du MH, Wang DY, et al. Highly fluorescent CdTe@SiO_2 particles prepared via reverse microemulsion method. Chem Mater 2010;22:420–7.
[71] Jing LH, Ding K, Kalytchuk S, Wang Y, Qiao R, Kershaw SV, et al. Aqueous manganese-doped core/shell CdTe/ZnS quantum dots with strong fluorescence and high relaxivity. J Phys Chem C 2013;117:18752–61.
[72] Iyer AK, Khaled G, Fang J, Maeda H. Exploiting the enhanced permeability and retention effect for tumor targeting. Drug Discov Today 2006;11:812–8.
[73] Liu JB, Yu MX, Zhou C, Yang SY, Ning XH, Zheng J. Passive tumor targeting of renal-clearable luminescent gold nanoparticles: long tumor retention and fast normal tissue clearance. J Am Chem Soc 2013;135:4978–81.
[74] Robinson JT, Hong G, Liang Y, Zhang B, Yaghi OK, Dai H. In vivo fluorescence imaging in the second near-infrared window with long circulating carbon nanotubes capable of ultrahigh tumor uptake. J Am Chem Soc 2012;134:10664–9.
[75] Choi HS, Liu W, Misra P, Tanaka E, Zimmer JP, Ipe BI, et al. Renal clearance of quantum dots. Nat Biotechnol 2007;25:1165–70.